THE JOURNAL OF PHYSICAL CHEMISTRY C

Article

pubs.acs.org/JPCC

Single Crystal Electron Paramagnetic Resonance with Dielectric Resonators of Mononuclear Cu^{2+} Ions in a Metal−Organic Framework Containing Cu_2 Paddle Wheel Units

Stefan Friedländer,[†] Mantas Šimėnas,[†,‡] Merten Kobalz,[§] Pierre Eckold,[§] Oleg Ovchar,[∥] Anatolii G. Belous,[∥] Jūras Banys,[‡] Harald Krautscheid,[§] and Andreas Pöppl*[,†]

[†]Abteilung für Magnetische Resonanz Komplexer Quantenfestkörper, Fakultät für Physik und Geowissenschaften, Universität Leipzig, Linnéstr. 5, 04103 Leipzig, Germany

[‡]Faculty of Physics, Vilnius University, Sauletekio 9, 10222 Vilnius, Lithuania

[§]Institut für Anorganische Chemie, Fakultät für Chemie und Mineralogie, Universität Leipzig, Johannisallee 29, 04103 Leipzig, Germany

[∥]Institute of General and Inorganic Chemistry, National Academy of Sciences of Ukraine, Academian Palladin Avenue 32−34, 03680 Kyiv, Ukraine

Supporting Information

ABSTRACT: Dielectric resonator aided sensitivity-enhancing electron paramagnetic resonance was successfully applied to small single crystals of the previously reported metal−organic framework compound $^{3}_{\infty}[Cu^{I}_{2}Cu^{II}_{2}(H_2O)_2L_2Cl_2]$ in a conventional X-band EPR spectrometer at 7 K sample temperature to reveal the nature of mononuclear Cu^{2+} ion defect species. We found that these paramagnetic defects are not related to an impurity phase or extraframework species of the parent metal−organic framework material but are formed within the framework. Novel angular resolved single crystal continuous wave electron paramagnetic resonance supported by powder measurements and single crystal X-ray diffraction on this metal−organic framework compound identified defective copper paddle wheel units with one missing Cu^{2+} ion as the observed mononuclear paramagnetic species in this compound. The sensitivity enhancement by an estimated factor of 8.6 for the single crystal electron paramagnetic resonance spectroscopy is required to efficiently record the Cu^{2+} ion signals in single crystals of typical sizes of 200 × 50 × 50 μm^3 at X-band frequencies. The results demonstrate that conventional electron paramagnetic resonance spectrometers operating at X-band frequencies and equipped with dielectric resonators can successfully be used to perform single crystal studies of these porous, low density materials with very small volume samples at low temperatures.

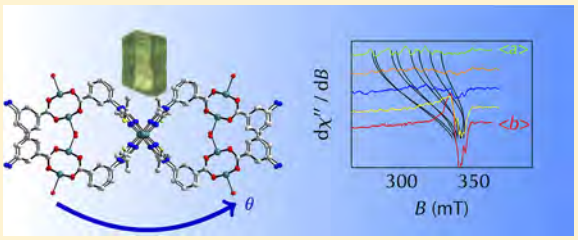

INTRODUCTION

Over the last decades, the interest in metal−organic frameworks (MOFs) as discrete class of porous solids has emerged.[1] MOFs, which are formed of metal centers and organic linkers, are dedicated for gas separation and storage[2] and reveal interesting properties for catalytic application.[3,4] A growing part of research is spent on the magnetic properties of MOFs,[5,6] such as the recently observed ferromagnetism in dinuclear Cu^{2+} based MOFs with $Cu_2(COO)_4$ paddle wheels (PWs).[7] Among other characterization methods, electron paramagnetic resonance (EPR) spectroscopy had been used to elucidate the nature of paramagnetic probes including their interaction with diamagnetic and paramagnetic adsorbates in MOFs as well as structural deformation processes upon gas adsorption.[8,9]

One of the most studied MOFs is the well-known HKUST-1.[10] It is based on PW secondary building units with two Cu^{2+} ions and forms a regular three-dimensional network of $[Cu_3(btc)_2(H_2O)_3]_n$ with defined cages and channels. The high porosity found in numerous studies set benchmarks for adsorption capabilities of MOFs and the effectiveness of separation of CO_2 and CH_4.[11] Despite the beneficial properties, a number of difficulties arise in large scale handling, among them instability against humid environments and low thermal resilience,[12] which make it worthwhile to synthesize and investigate novel compounds. Therefore, a MOF material with the chemical formula $^{3}_{\infty}[Cu^{I}_{2}Cu^{II}_{2}(H_2O)_2L_2Cl_2]$ (**1**) was prepared by solvothermal synthesis.[13] Here, L stands for 3,3′-(5,5′-(thiophene-2,5-diyl)bis(3-methyl-4*H*-1,2,4-triazole-5,4-diyl))dibenzoate).

The structure of this MOF determined by single crystal X-ray diffraction (XRD) analysis was discussed in a previous report.[13] A presentation of the network with space group $I2_12_12_1$ is

Received: May 26, 2015
Revised: July 30, 2015
Published: July 30, 2015

DOI: 10.1021/acs.jpcc.5b05019
J. Phys. Chem. C 2015, 119, 19171−19179

shown in Figure 1. The three-dimensional network contains both Cu^{+} and Cu^{2+} ions. The Cu^{2+} ions build PW units

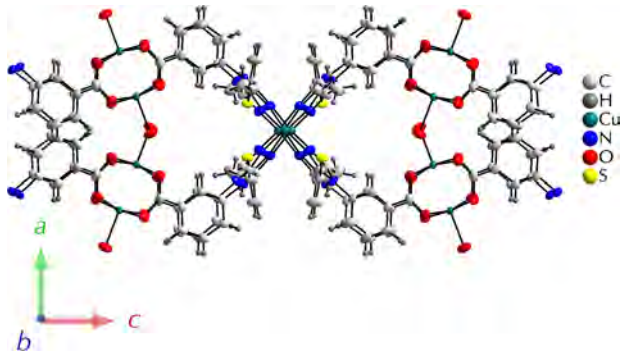

Figure 1. Ball-and-stick presentation of $^{3}_{\infty}[Cu^{I}_{2}Cu^{II}_{2}(H_2O)_2L_2Cl_2]$.

coordinated by four carboxylate groups of the ligand L and two water molecules on the apical positions. The Cu^{+} ions are coordinated by four nitrogen atoms of four bridging triazole rings resulting in a tetrahedral coordination environment. Synthesis, crystal structure, and powder continuous wave (cw) EPR spectroscopy data of the MOF have been described recently.[13]

It was found that the Cu^{2+} ions in Cu/Cu PW units are coupled antiferromagnetically and have an excited $S = 1$ electron spin state and an EPR silent $S = 0$ ground state.[14] The observed coupling is a direct consequence of the superexchange of two unpaired electrons residing in a single Cu/Cu PW unit. Moreover, a pronounced interdinuclear exchange of the excited spin triplets between neighboring Cu/Cu PW units in the dehydrated MOF has been reported.[13] In addition, the cw EPR experiments revealed mononuclear Cu^{2+} ion species of unknown origin.

The elucidation of the origin of such mononuclear Cu^{2+} ions in MOFs containing Cu/Cu PW units seems to be a general problem, since minor mononuclear Cu^{2+} species have also been observed in HKUST-1,[8,14] $[Zn_{1-x}Cu_x(bdc)\ (dabco)]_{0.5}$,[15] and STAM-I MOFs[16] and were attributed to extraframework impurities in high local concentrations from untransformed reactants. However, in many cases a direct proof about the origin of these cupric ion defect species has not been provided. In this study, we focus on cw EPR of powder materials and single crystals of the mononuclear Cu^{2+} ion species in the as-synthesized **1**. The latter method is often not feasible in MOF research due to the small size of available single crystals and the consequently very low spin number and related intensity of the EPR signals obtained for these porous, low density solids.

Very small samples have become customary for application in high-field EPR which makes use of the high filling factors from the regularly small resonant cavities of, for example, the W-band resonators.[17] However, dedicated EPR studies on MOF crystals with dimensions below some hundred μm edge length are not frequently reported. Presumably, the insufficient sensitivity of conventional X-band cw EPR experiments employed in MOF research prevented such investigations so far. Therefore, our experiments involve dielectric resonator (DR) based cw EPR on small single crystals in addition to conventional setups for cw EPR on MOF powder samples. DRs are an easy and convenient way to improve the signal-to-noise ratio (SNR) in conventional EPR spectrometers and have been applied widely for a long time.[18−21] Novel DRs with low concentration of paramagnetic impurities and high dielectric permittivities provide an easy-to-use setup for commercial spectrometers, where the DR is placed in a typical EPR sample tube together with the studied sample to perform experiments at temperatures below 77 K.[22] Here we describe the application of these DRs for single crystal MOF cw EPR studies and present the advantages of their usage compared to measurements in conventional cavity resonators at X-band frequencies. With these experiments together with studies on MOF powders, we were able to determine both the principal values and the orientation of the principal axes of the **g** tensor and hyperfine splitting (HFS) tensor **A** of the mononuclear Cu^{2+} species in **1** by EPR. In particular, the principal axes of the interaction tensors can be related with the crystal structure obtained from XRD. This enabled us to identify the nature of the mononuclear Cu^{2+} species in a superior way compared to previous reports and propose an improved model for the structure of this framework.

EXPERIMENTAL METHODS

Single Crystal Preparation. $^{3}_{\infty}[Cu^{I}_{2}Cu^{II}_{2}(H_2O)_2L_2Cl_2]$ was prepared by solvothermal synthesis with H_2O/MeCN (water/acetonitrile, volume ratio 1:1) as a solvent as described previously and corresponds to sample **1** therein.[13] The obtained crystals have a maximum length of about 200 μm along the crystallographic *b* axis and up to 50 μm in *a* and *c* directions. The latter two are well distinguishable due to the typical rooftop tails of the short needles. Crystal axis assignment for single crystals of **1** was performed using a STOE IPDS-2T image plate detector system with laboratory Mo Kα radiation (λ = 71.073 pm). The data were processed with the STOE X-AREA software.[23] Diamond 3.2f was used to visualize the structures.[24]

The investigated as-synthesized single crystal sample is shown in Figure 2a. The green specimen is placed with its flat

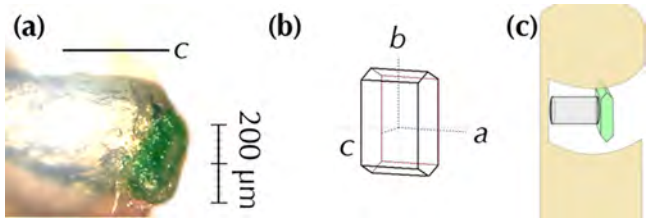

Figure 2. (a) Single crystal of **1** taken for all experiments reported. (b) Depicted crystal outline with crystallographic axes indicated. (c) Sketch of the beveled quartz glass rod with 1 mm diameter housing the crystal glued to the fiber.

ab face on a quartz glass fiber end with 300 μm diameter such that the *c* axis is pointing along the axis of the wire. The crystal is fixed and covered with two component epoxy which neither has a measurable effect on the crystal lattice according to XRD nor gives any detectable EPR resonances. This glue maintains the crystal's stability under multiple cooling and warming processes and is therefore crucial for our series of single-crystal EPR experiments of **1**. Figure 2b shows the depicted crystal shape with the crystal axes assignment. To enable modification of the alignment of the crystal with respect to the DR and the external magnetic field in the cryostat, an impurity free quartz glass rod of 1 mm diameter was beveled to house the crystal on its glass fiber as shown in Figure 2c. This rod fits in the hole of

DOI: 10.1021/acs.jpcc.5b05019
J. Phys. Chem. C 2015, 119, 19171−19179

the DR as described later and places the crystal almost exactly in the radial and lateral middle of the DR.

Single Crystal and Powder cw EPR. The cw EPR measurements at X-band frequencies were carried out using a BRUKER EMXmicro X-band spectrometer equipped with a BRUKER ER 4119HS cylindrical cavity resonator and an OXFORD ESR 900 flow cryostat for low temperature measurements. The Q-band cw EPR spectra were recorded with a BRUKER EMX 10−40 spectrometer operating at 34 GHz. For single crystal measurements at low temperatures and X-band frequencies, DRs of the type K80-H on the basis of barium lanthanide titanates solid solutions (BLTss) with the general formula $Ba_{6-x}Ln_{8+2x/3}Ti_{18}O_{54}$ (Ln = Sm, Nd) have been employed.[22,25] The single crystal sample must be easily orientable in three dimensions and in order to achieve that it is placed in differently bevelled quartz glass rods as shown in the Supporting Information (SI).

One single crystal was used to investigate the angular dependence of the EPR spectra for rotations about three distinct axes. These axes were chosen to be preferably parallel to the crystal axes *a*, *b*, and *c*. Due to the distinct needle shaped crystal, it was possible to specifically select the intended orientations, yet with a systematic error of at least ±5° for various reasons. First, the crystal faces are not perfectly aligned with the glass fiber. Second, the glass fiber has not been oriented ideally in the beveled glass rod. Moreover, the glass rod is not fully erected along the DRs symmetry axis and the DR is not entirely correctly aligned in the resonator, a compromise devoted to the easy setup allowing for fast sample changes. Then the crystal was rotated by the angle φ about one of the chosen axes, each in steps of $\Delta\varphi = 5°$. This angle may have a systematic error of up to $\Delta_{err}\varphi = 5°$, too. The rotations were started at about $\varphi_0 = -30°$ before a characteristic signal occurrence and followed up for at least 220° to meet all signals occurring for a C_2 rotational symmetry. Typically, only two accumulations were taken per spectrum, and for selected angles repeated scans with up to 40 scans were taken to ensure a safe signal detection. The single crystal spectra were recorded with very low power of 60 μW, the powder spectra on the same spectrometer setup without DR with higher power of 2 mW at 7 K sample temperature. All cw EPR spectra were recorded with a modulation strength of 5G and frequency of 100 kHz. Analysis of the EPR spectra has been facilitated by the EasySpin numerical simulation package for MATLAB.[26]

RESULTS

XRD. During refinement of the crystal structure of **1** based on single crystal XRD data, a peculiarity concerning the Cu^{2+} ions was observed. In contrast to the Cu^{+} ions, the anisotropic displacement factors for the Cu^{2+} ion were slightly increased. In order to investigate the origin of this deviation, the site occupancy factors (sof) of Cu^{2+} and Cu^{+} ions were refined. Whereas the sof of the Cu^{+} ions were found to be 0.49 and 0.50, respectively (positions of Cu^{+} ions are located on 2-fold axes; expected sof, 0.50), the sof for the Cu^{2+} ion is refined to 0.933(4). A possible explanation for this observation is the presence of "defective" PW units, in which only one Cu^{2+} position is occupied. Based on the XRD data, about 13% of all PWs would be defective.

Powder EPR. Figure 3 shows the obtained powder spectrum of **1** measured at X-band frequency and 7 K sample temperature around values of the *g*-factor $g = 2$. The experimental spectrum in Figure 3a (upper two lines, red)

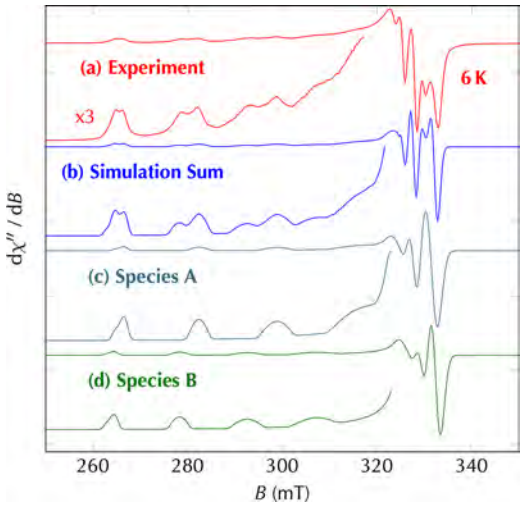

Figure 3. (a) Experimental powder spectrum at 7 K. (b) Sum of the simulated spectra of the two mononuclear species. Simulated spectra of (c) species A and (d) species B.

shows the well-known anisotropic EPR powder pattern of mononuclear Cu^{2+} ions with $S = 1/2$ electron spin interacting with the nuclear magnetic moments of the ^{63}Cu and ^{65}Cu isotopes with nuclear spin $I = 3/2$ each. The excited $S = 1$ spin state resonance lines of the antiferromagnetically coupled Cu^{2+} pair in the PW units are not present in the spectrum due to the low temperature of 7 K. In the spectrum, two different patterns assigned to two axially symmetric Cu^{2+} species A and B can be identified in accordance to the previous report.[13] Both species show well resolved HFS signals in the $g_{\|}$ part or their powder pattern, indicating only moderate strain effects. The spectrum of each species can be simulated using the spin Hamiltonian which includes electron Zeeman and hyperfine interactions:

$$\mathcal{H}_i = \beta_e \mathbf{B}_0 \mathbf{g}_i \mathbf{S} + \mathbf{S}\mathbf{A}_i\mathbf{I} \quad (1)$$

Here the subscript i marks species A or B. $\mathbf{g}_i$ denotes the **g** tensor and $\mathbf{A}_i$ the HFS tensor of the respective copper nucleus, and the total spin Hamiltonian is the sum of both Hamiltonians $\mathcal{H}_i$. Though strain effects are moderate, the increasing line widths of the HFS signals in the $g_{\|}$ part with increasing field for both Cu^{2+} species are typical for correlated *g* and *A* strain distributions.[27] Consequently, such a correlated Gaussian *g* and *A* strain distribution have been taken into account in the simulation of the EPR powder patterns of the Cu^{2+} species A and B (see the SI). The simulations revealed almost equal intensities for both species with axially symmetric and collinear **g** and **A** tensors. The principal values of the axially symmetric **g** and **A** tensors of species A and B in the here studied as-synthesized sample as obtained by the simulations are given in Table 1.

Mononuclear Cu^{2+} Concentration. In addition to the mononuclear Cu^{2+} ion signal, the fine structure pattern of Cu/Cu PW units (two exchange coupled Cu^{2+} ions result in a total

Table 1. Simulation Parameters for the Mononuclear Cu^{2+} Species

parameter	species A	species B
$g_{\|}$, $g_{\perp}$	2.317(2), 2.055(5)	2.359(2), 2.044(5)
$A_{\|}$, $A_{\perp}/10^{-4}$ cm^{-1}	173(1), 18(2)	153(1), 18(2)

DOI: 10.1021/acs.jpcc.5b05019
J. Phys. Chem. C 2015, 119, 19171−19179

spin $S = 1$) appears at temperatures above 50 K allowing us to determine the ratio between the number of mononuclear Cu^{2+} species and Cu^{2+} pairs in Cu/Cu PW units.[13] We used the following procedure to determine this ratio. First of all, it is known that the EPR signal intensity I is proportional to the magnetic susceptibility χ,[28] that is, $I = K\chi$, where K is a function of the quality and the filling factors of the resonator as well as the mw power.[29] Second, it is justified to assume that K is the same for the mononuclear and dinuclear Cu^{2+} centers. However, the temperature dependence of χ of these two species differs significantly. The susceptibility of mononuclear Cu^{2+} centers χ_M at relatively high temperatures obeys the Currie law[30]

$$\chi_M = \frac{N_M}{4}\frac{\beta_e^2 g_M^2}{k_B T} \tag{2}$$

where N_M and g_M denote the number and effective g value of mononuclear Cu^{2+} centers, respectively. In contrast, in the case of Cu/Cu PW units, it is governed by the Bleaney−Bowers equation[31]

$$\chi_{PW} = 2N_{PW}\frac{\beta_e^2 g_{PW}^2}{k_B T}\left[3 + \exp\left(\frac{-J}{k_B T}\right)\right]^{-1} \tag{3}$$

Here, J is the exchange coupling constant (exchange Hamiltonian $\mathcal{H} = -JS_1S_2$), which was determined in a previous report to be -278 cm^{-1}.[13] N_{PW} and g_{PW} are the number and g value of Cu/Cu PWs, respectively. Finally, neglecting small differences between the g values for both species, one obtains the following expression for the ratio between EPR signal intensities of mononuclear and dinuclear species:

$$\frac{I_M}{I_{PW}} = \frac{\chi_M}{\chi_{PW}} = \frac{1}{8}\frac{N_M}{N_{PW}}\left[3 + \exp\left(\frac{-J}{k_B T}\right)\right] \tag{4}$$

Thus, if J is known, then one can estimate the ratio N_M/N_{PW} just by measuring a single spectrum. In our case, the spectrum was measured at Q-band frequency and at $T = 295$ K (Figure 4). The higher spectrometer frequency allowed us to obtain the complete fine structure pattern of the $S = 1$ state of the Cu/Cu PW units. The intensities I_{PW} and I_M were determined by double integration of the simulated signals shown in Figure 4c and d, respectively. The spin Hamiltonian parameters used for simulating the fine structure pattern are the same as those in ref 13, $g_\perp = 2.072(2)$, $g_\parallel = 2.383(2)$, $D = -0.355(1)$ cm^{-1}, and $E \approx 0$. In such a way, we obtained the ratio $N_M/N_{PW} = 0.11(2)$. From this, we estimate a net spin number of 10^{13} mononuclear Cu^{2+} EPR spins in the single crystal of **1** with the size of $200 \times 50 \times 50$ μm^3. The ratio $N_M/N_{PW} = 0.11(1)$ is also in excellent agreement with an improved analysis (see SI) of magnetic susceptibility measurements of **1**.[13]

Single Crystal EPR. Figure 5a shows the experimental single crystal spectrum with 40 accumulations and the $\mathbf{B}_0$ field vector in the *ac* plane with ±5° uncertainty for this experiment. The crystal is oriented such that its *a* axis and the direction of $\mathbf{B}_0$ form an angle of 20°. The spectrum displays a number of distinct, angular dependent Cu^{2+} EPR signals of varying width and resolution. The poor spectral resolution and the low SNR in the experiment must be explained by the low spin number with respect to the resonator sensitivity in general and line broadening effects among others caused by correlated g and A strain as in the powder EPR spectra (cf. Figure 3) such that the

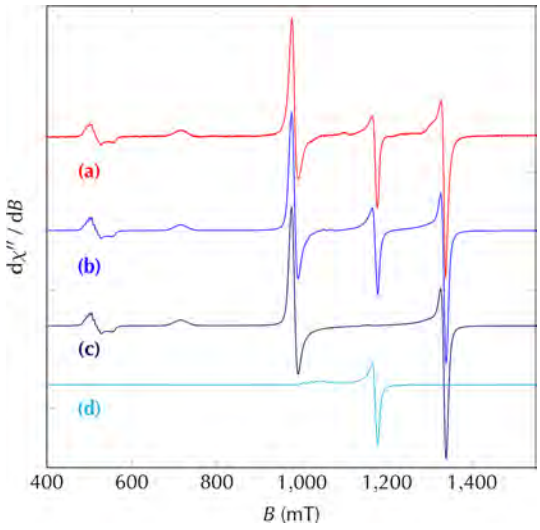

Figure 4. Q-band cw EPR powder spectrum of **1** at room temperature: (a) experimental spectrum, (b) sum of simulations, (c) simulation of PW fine structure pattern, and (d) simulation of mononuclear Cu^{2+} ion signal.

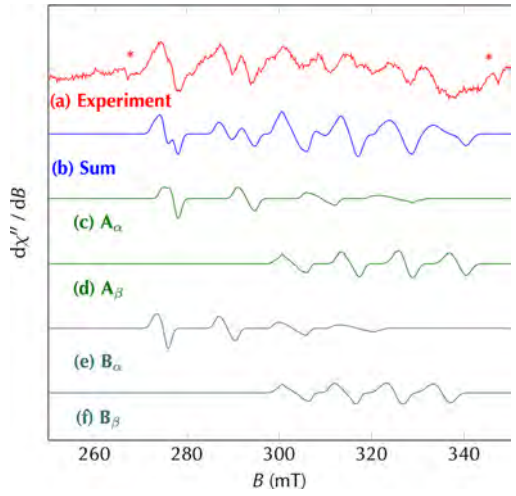

Figure 5. (a) Experimental single crystal spectrum at 7 K, $\mathbf{B}_0$ in *ac* plane, the angle of $\mathbf{B}_0$ with the *a* axis is 20(5)°, the asterisks mark artifacts from background subtraction. (b) Sum of simulated spectra. Simulated spectra of species (c) A_α, (d) A_β, (e) B_α, and (f) B_β.

EPR lines in the high field region are broader compared to those in the low field part and are consequently less resolved (see the SI). The simulated spectra in Figure 5b−f will be explained in more detail below. An example of a complete angular dependence of the single crystal of **1** with $\mathbf{B}_0$ rotated in the *ac* plane (determined with an accuracy of ±5°) is shown in Figure 6. The resonance fields vary from $B = 290$ mT, which corresponds to the parallel part of the powder spectrum of **1**, to $B = 340$ mT, representing the perpendicular part of the corresponding powder spectrum. The shown angular dependence resembles a 2-fold symmetry for the rotation in the *ac* plane about the angle φ with respect to the respective crystallographic axes. Experimental spectra for rotations in the other two planes are shown in the SI. Overall, four angular-dependent sets of the four $S = 1/2$, $I = 3/2$ single crystal copper HFS resonance field lines can be identified. Two sets of resonance lines, denoted by A and B, follow the same angular dependence (α or β), each, but with slightly different resonance

DOI: 10.1021/acs.jpcc.5b05019
J. Phys. Chem. C 2015, 119, 19171−19179

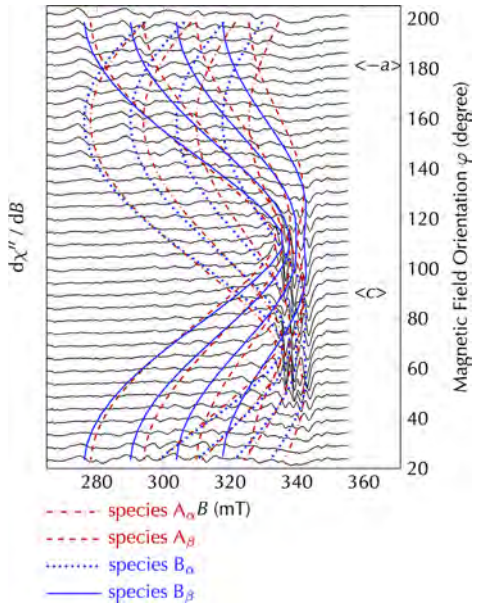

Figure 6. Angular dependent EPR spectra of the single crystal of **1** for a rotation of the magnetic field vector $\mathbf{B}_0$ in the *ac* plane with ±5° accuracy for all angles. The colored and differently dashed lines mark the four sets of simulated resonance fields of the two species A and B, each for the two tensor orientations α and β.

positions and hyperfine splittings and reach their maximum respective copper HFS and effective *g* values under an angle of $\varphi = \pm (20 \pm 5)°$ with the *a* axis. We assign these two distinct sets of resonance lines to the two mononuclear Cu^{2+} species A and B observed in the EPR powder spectra of **1**. Consequently, the species (A_α, A_β, and B_α, B_β) with distinct angular dependencies are assigned to two orientations α and β of their **g** and **A** tensors, representing two magnetically nonequivalent, symmetry related, incorporation sites of the mononuclear Cu^{2+} species A and B. The rotations in the other two planes shown in the SIprovide only one set of copper HFS lines for each species A and B, indicating that the projections of the tensor orientations α and β onto the *ab* and *bc* plane are equivalent. The complete angular dependent resonance fields measured in three orthogonal planes are summarized in Figure 7. It is reasonable to use the principal values of the **g** and **A** tensors of the two species A and B which are found in the respective powder spectrum (Table 1) to fit simultaneously these three single crystal angular dependencies. The fit yields the angles $\theta^{\alpha,\beta}_{a,b,c}$ of the principal axis *z* of the **g** and **A** tensors of the species A_α, A_β, B_α, and B_β with respect to the crystal axes *a*, *b*, and *c* of the orthorhombic unit cell. Here the *z* axes correspond to the symmetry axis of the two magnetic tensors. We determine the angles $\theta^{\alpha,\beta}_a = \pm 20(5)°$, $\theta^{\alpha,\beta}_b = 90(5)°$, and $\theta^{\alpha,\beta}_c = \pm 70(5)°$ of the two tensor orientations assigned to the two magnetically inequivalent incorporation sites of both species A and B. Figures 6 and 7 show that for all three planes the experimentally read off resonance fields fit well enough to the computed angular dependencies (red and blue lines) using the obtained angles $\theta^{\alpha,\beta}_{a,b,c}$ and the principal values from Table 1.

Discrepancies between the experimentally obtained and computed resonance fields in the angular dependencies are caused by different error contributions: at first, in the experiment, we must assume a systematic uncertainty of about 5° of all orientations with respect to the indicated angles. Second, we observe line broadening effects by correlated *g* and *A* strain in the powder EPR spectra (see Figure 3). Therefore, likewise in the single crystal spectra, the resonance field lines in the high field region are broader compared to those at low fields. Consequently, resonance fields of the low field signals must be considered to be more reliable for the analysis of the angular dependency. Finally, the asymmetric experimental line shape due to insufficient background subtraction, line broadening effects and the general low SNR as seen in the detailed background subtracted single crystal spectrum previously shown in Figure 5a introduce an appreciable uncertainty of up to 1.5 mT in the determination of the resonance field positions. After all, regarding these error contributions the simulated resonance field positions reproduce the experimental observations with acceptable accuracy.

Using the principal values of the **g** and **A** tensors of the two Cu^{2+} species A and B (Table 1) and the above determined angles $\theta^{\alpha,\beta}_{a,b,c}$ of the tensor *z* axes with the crystallographic axes we can now simulate the single crystal spectrum in Figure 5b with $\mathbf{B}_0$ in the *ac* plane. The spectrum is composed by a superposition of the EPR spectra of the four species A_α, A_β, B_α, and B_β which correspond to the two magnetically nonequivalent sites of species A and B with tensor orientations α and β. In the simulation of the single crystal spectra we employed again a correlated *g* and *A* strain line broadening model using the same parameters as for the simulation of the powder pattern (see the SI). This line broadening model may also account for the increasing line widths of the copper HFS signals in the single crystals spectrum in going from lower

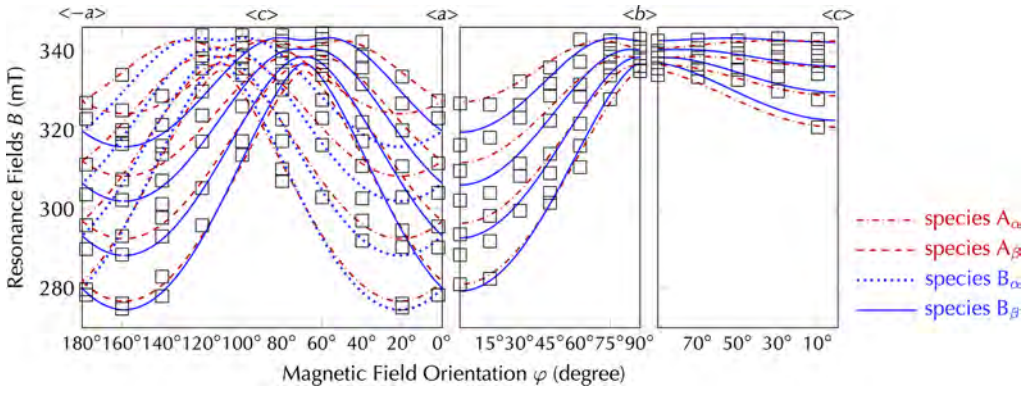

Figure 7. Angular dependent resonance field positions of the mononuclear Cu^{2+} species measured in three orthogonal planes (the size of the black open squares resembles error limits) and the simulated angular dependencies of the single crystal of **1** (red, blue lines).

DOI: 10.1021/acs.jpcc.5b05019
J. Phys. Chem. C 2015, 119, 19171−19179

toward higher magnetic fields. But in addition, we observe that the low field HFS line of the species A_β and B_β are more broadened than those of A_α and B_α, indicating the presence of a further line broadening mechanism. For the given orientation, the magnetic field $\mathbf{B_0}$ is approximately parallel to the symmetry axis of the **g** and **A** tensors for the tensor orientation α (species A_α, B_α), whereas it forms an angle of 40° for the tensor orientation β. As the latter orientation is more affected by this second line broadening effect, we propose a Gaussian distribution of the angles $\theta_a^{\alpha,\beta}$ and $\theta_c^{\alpha,\beta}$ with a small distribution width $\Delta\theta \approx 2.4°$. Indeed, taking into account both line broadening mechanisms, we can simulate the single crystal spectrum in Figure 5a by a superposition of the EPR signals of all four species in Figure 5c–f, namely A_α, A_β, B_α, and B_β with satisfying agreement. In the simulation, we assumed identical intensities for species A and B, although in general the intensity ratio of species A and B may vary to certain extend among different crystals. In the low field region of Figure 5a, it is easy to identify the resonance fields while at higher fields (300–340 mT) the resonance lines are broader, less well resolved and rather asymmetric. This explains also why the accuracy in the determination of the resonance fields in the range 300–340 mT is limited and leads to some discrepancies between experimental and computed angular dependencies of the resonance fields in that field range (Figure 7).

After all, we have identified two approximately equally populated, axially symmetric Cu^{2+} species A and B that are incorporated at two magnetically inequivalent, symmetry related sites (tensor orientations α, β) into the framework of **1**.

DISCUSSION

The cw X-band EPR data reveal the presence of two distinct mononuclear Cu^{2+} species A and B in $^3_\infty[Cu^I_2Cu^{II}_2(H_2O)_2L_2Cl_2]$ (**1**). EPR measurements on single crystals provided clear 2-fold angular dependencies of their corresponding resonance fields. This can be linked to the crystal structure of **1** with space group $I2_12_12_1$ with perpendicular screw axes along the three crystallographic axes leading to two magnetically nonequivalent, symmetry related sites. Hence, the obtained angular dependency mirrors the crystal structure of **1**. Therefore, we conclude that species A and B are located at well-defined sites within the MOF crystallites of **1** and are not formed in a minor amorphous impurity phase. Moreover, the well resolved EPR powder patterns of A and B with only minor correlated *g* and *A* strain effects suggest an incorporation of the mononuclear cupric ion species at well-defined lattice sites. For instance the Cu^{2+} ions in the Cu/Zn PW units of a partially zinc substituted HKUST-1 MOF exhibit likewise EPR powder patterns of superior resolution without any noticeable strain effects.[32] Otherwise, extraframework Cu^{2+} species usually give rise to poorly resolved powder spectra due to substantial *g* and *A* strains or high local concentrations.[14]

There are three distinct metal ion sites in the framework of **1**, two Cu(I) sites each with a distorted tetrahedral coordination to four nitrogen atoms and the Cu(II) sites in the Cu/Cu PW units which have a local C_4 symmetry axis along the Cu–Cu direction. In these Cu/Cu PW units, the cupric ions are coordinated by four basal oxygen atoms of bridging carboxylate groups of the ligands and an apical oxygen atom of the axially coordinating solvent water molecule in a square pyramidal coordination symmetry (Figure 1). The two magnetically nonequivalent, symmetry related PW orientations are formed by the screw axes in *a*, *b*, and *c* direction of space group $I2_12_12_1$.

Although it is usually not possible to deduce from the principal values of the Cu^{2+} **g** and **A** tensors the exact metal ion coordination geometry, the g_{zz} and A_{zz} parameters of the cupric ion species provide a rough guide to the overall coordination geometry of the metal ion site. Based on a number of studies of Cu^{2+} ions in an oxygen coordination environment, A_{zz} increases from ~0.007 cm^{-1} for tetrahedral symmetry, through elongated distorted octahedral symmetry with ~0.0130 cm^{-1}, square pyramidal, and trigonal pyramidal to ~0.0190 cm^{-1} for square planar symmetry, whereas g_{zz} decreases from 2.516 to 2.245 for this sequence of coordination symmetries.[33,34] So the values of $g_{zz} \sim 2.42$ and $A_{zz} \sim 0.0130$ cm^{-1} indicate a distorted octahedral coordination of the Cu^{2+} ions to six oxygen atoms,[35] but $g_{zz} \sim 2.279$ and $A_{zz} \sim 0.0190$ cm^{-1} suggest rather a square planar coordination.[32] In the case of a coordination of the cupric ion to four nitrogen atoms, a transformation from a tetrahedral to a planar coordination symmetry is accompanied by change from $g_{zz} \sim 2.32$ and $A_{zz} \sim 0.0080$ cm^{-1} to $g_{zz} \sim 2.18$ and $A_{zz} \sim 0.0200$ cm^{-1}.[36] The obtained parameters g_{zz} and A_{zz} of two distinct mononuclear Cu^{2+} species A and B in Table 1 indicate a square pyramidal oxygen environment. Indeed, comparable Cu^{2+} spin Hamiltonian parameters have been reported for cupric ions with axially coordinating water or methanol molecules in Cu/Zn PW units of a partially zinc substituted HKUST-1 MOF. Furthermore, both tensors **g** and **A** are axially symmetric within the experimental accuracy in accordance with a square pyramidal coordination of the Cu^{2+} ions.[32] Therefore, and for other chemical aspects, we may rule out that the two Cu^{2+} species A and B are formed by oxidation of Cu(I) with their distorted tetrahedral nitrogen coordination. We rather assume the formation of defective Cu/Cu PW units with one missing cupric ion as illustrated in Figure 8.

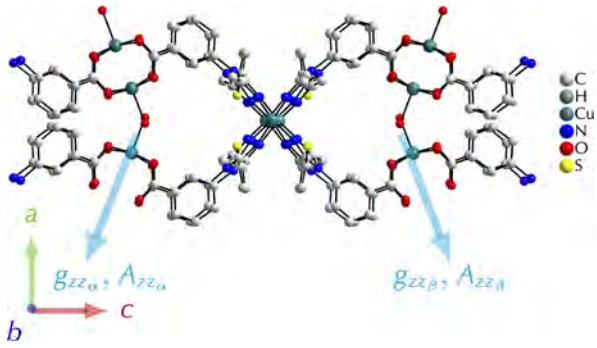

Figure 8. Projection of **1** with two magnetically nonequivalent intact and two defective PW units. The vectors indicate the two possible orientations α and β of the *z* principal axes of the tensors **g** and **A**.

In that case, the *z* principal axes of the **g** and **A** tensors of the metal ion shall be directed along the local C_4 symmetry axis of the former Cu/Cu PW unit. Our angular dependent EPR measurements on small single crystals of **1** confirm this assignment. The C_2 symmetry in the angular dependent spectra can be explained fully with the two magnetically nonequivalent sites for the Cu/Cu PW units related via the 2_1 screw axes in the crystal structure of **1** with space group $I2_12_12_1$ as illustrated in Figure 8. For both sites, the local C_4 symmetry axis of the Cu/Cu PW units are oriented parallel to the crystallographic *ac* plane and form an angle with the *a* lattice axis of about ±21°. Table 2 compares the angles θ_a, θ_b, and θ_c between the C_4 symmetry axis of the Cu/Cu PW units and the lattice axes with

DOI: 10.1021/acs.jpcc.5b05019
J. Phys. Chem. C 2015, 119, 19171–19179

Table 2. Angles $\theta^{\alpha,\beta}_{a,b,c}$ of z Principal Axis of g and A Tensors of Mononuclear Cu^{2+} Ions with Respect to Unit Cell Axes and Directions of the Local C_4 Symmetry Axis r of the Cu/Cu PW Units As Defined by the Vector Pointing from One to the Other Cu^{2+} Ion in the PW Unit

angle	$\theta^{\alpha,\beta}_a$	$\theta^{\alpha,\beta}_b$	$\theta^{\alpha,\beta}_c$
r	±20.88°	90°	∓69.12°
z	±20(5)°	90(5)°	∓70(5)°

those angles the z principal axes of the **g** and **A** tensors of the two Cu^{2+} species A and B form with the lattice axes for the two tensor orientations α and β. Both sets of angles with the lattice axes are in good accordance taking into account the experimental errors of the determined angles of the z principal axes of the two tensors. The direction of the z principal axes of the tensors **g** and **A** deviates only by $\angle(z, \mathbf{r}) = 5.1(5)°$ from the C_4 symmetry axis **r** of the Cu/Cu PW units. Moreover, EPR angular dependencies and the obtained two orientations α and β of the **g** and **A** tensors are in accordance with the two magnetically nonequivalent sites of the PW units (Figure 8) and reflect the crystal symmetry of **1**.

The suggested defect model for the mononuclear Cu^{2+} species A and B of a defective PW unit with one missing cupric ion is supported by the results of XRD measurements and relative EPR intensity measurements. The XRD refinement of the crystal structure of **1** gave a site occupancy factor of 0.933(4) for cupric ions in PW units. Consequently, approximately 13% of the PW units are defective with one missing cupric ion. The analysis of the relative intensities in the EPR powder spectra of **1** provide a ratio between the mononuclear Cu^{2+} species, in that case the defective PW units, and the intact Cu/Cu PW units. This ratio of 0.11 corresponding to about 10% defective PWs with respect to all PW units is in good accordance with the XRD sof-analysis. The approximately 10% of defective PWs must be compared to 0.01% of the PWs located at the surface of a single crystal with these dimensions which supports the rejection of the dangling-bond model from surface states.

Our proposed defective PW unit model accounts well for the EPR results of both powder and single crystal studies of **1** as well as the XRD refinement of the crystal structure. However, we may only speculate about the occurrence of two mononuclear Cu^{2+} species A and B with the identical orientations of the principal axes frames of their **g** and **A** tensors but with distinct principal values. The latter indicate slightly different coordination environments of the two cupric ion species presumably caused by some minor but well-defined deformations of the defective PW units. One possible explanation might be that a defective PW unit with one missing Cu^{2+} ion carries a 2-fold negative charge that must be compensated for instance by the protonation of the non-bonding oxygen atoms of the carboxylate groups. The required two protons may bind to either two adjacent or two opposite lying oxygen atoms leading to two slightly different coordination environments of the Cu^{2+} ion in the defective PW unit. Otherwise, a removal of the axial water ligand to the cupric ions in the PW units or its substitution by another polar solvent molecule may lead to a modification of the axial ligand field at the metal ion and consequently likewise to a small change in the g_{zz} and A_{zz} principal values of the tensors **g** and **A**.[37] In both scenarios, the changes to the coordination symmetry of the cupric ion are expected to be small so that the axial symmetry of the **g** and **A** tensors and its orientation are conserved within our experimental accuracy. It must be noted that the **g** and **A** parameters of the two species in the compound $^3_\infty[Cu^I_2Cu^{II}_2(H_2O)_2L_2Cl_2]$ are very sensitive to minor structural changes of the framework induced for example by different activation procedures.[13] This shows the sensitivity of both tensors with respect to small changes in the coordination environment of the Cu^{2+} ions in the defective PW units.

CONCLUSIONS

All single crystal measurements have been performed in a conventional X-band EPR spectrometer at 7 K sample temperature using DR aided sensitivity-enhancing cw EPR. The successful application of this technique at nonambient temperatures demonstrates the feasibility and potential of EPR spectroscopy on conventional X-band EPR spectrometers for the study of small single crystals even of porous, low density MOF materials. By comparative measurements, we confirmed the sensitivity enhancement by an estimated factor of 8.6 based on earlier studies[22] and could show the DRs are nevertheless mandatory to study successfully mononuclear Cu^{2+} centers in MOF single crystals of typical sizes of 200 × 50 × 50 μm^3.

We found relatively well identifiable, distinct, angular dependent EPR spectra of mononuclear Cu^{2+} ion species in single crystals of the framework $^3_\infty[Cu^I_2Cu^{II}_2(H_2O)_2L_2Cl_2]$ and deduced an ordered origin from a crystalline phase of these signals. We verified this angular dependency at three different rotations of $\mathbf{B}_0$ in the crystallographic *ab*, *bc*, and *ac* plane. The recorded spectra are sufficient to identify two species A and B of the mononuclear Cu^{2+} in two magnetically nonequivalent sites each. The angular dependencies can be fitted by the principal values of the **g** and **A** tensors of the species A and B as determined from the corresponding EPR powder spectra and the determined orientations α and β of the z principal axes of the magnetic tensors allow an assignment to defective PW units with one missing Cu^{2+} ion. On the basis of EPR intensities of powder materials and XRD studies of single crystals, we suggest that about 10% of the PW units are defective in the MOF structure.

The results demonstrate that cw X-band EPR can help to explore defect sites in MOF compounds and open an interesting field of high-sensitivity MOF single crystal studies using conventional EPR spectrometers.

ASSOCIATED CONTENT

Supporting Information

CCDC 1402768 containing the supplementary crystallographic data can be obtained free of charge from the Cambridge Crystallographic Data Centre via http://www.ccdc.cam.ac.uk/data_request/cif. The Supporting Information is available free of charge on the ACS Publications website at DOI: 10.1021/acs.jpcc.5b05019.

Explanation for application of DRs in this work, additional spectra for rotations of the single crystal of **1** about the *ab* and *bc* plane, and a description of the defect PW orientation (PDF)

AUTHOR INFORMATION

Corresponding Author

*Phone: +49 (0)341 9732608. Fax: +49 (0)341 9732649. E-mail: poeppl@physik.uni-leipzig.de.

DOI: 10.1021/acs.jpcc.5b05019
J. Phys. Chem. C 2015, 119, 19171−19179

Notes

The authors declare no competing financial interest.

■ ACKNOWLEDGMENTS

The authors gratefully acknowledge financial support within the priority programs SPP 1362 (Poröse metallorganische Gerüstverbindungen) and 1601 (Increasing Sensitivity with EPR) of the Deutsche Forschungsgemeinschaft (DFG). M.Š. thanks DAAD for the financial support.

■ REFERENCES

(1) Janiak, C.; Vieth, J. K. MOFs, MILs and more: concepts, properties and applications for porous coordination networks (PCNs). *New J. Chem.* **2010**, *34*, 2366−2388.
(2) Hartmann, M.; Kunz, S.; Himsl, D.; Tangermann, O.; Ernst, S.; Wagener, A. Adsorptive separation of isobutene and isobutane on $Cu_3(BTC)_2$. *Langmuir* **2008**, *24*, 8634−8642.
(3) Corma, A.; Garcia, H.; Llabrés i Xamena, F. Engineering metal organic frameworks for heterogeneous catalysis. *Chem. Rev.* **2010**, *110*, 4606−4655.
(4) Schlichte, K.; Kratzke, T.; Kaskel, S. Improved synthesis, thermal stability and catalytic properties of the metal-organic framework compound $Cu_3(BTC)_2$. *Microporous Mesoporous Mater.* **2004**, *73*, 81−88.
(5) Zhang, X. X.; Chui, S. S.-Y.; Williams, I. D. Cooperative magnetic behavior in the coordination polymers $[Cu_3(TMA)_2L_3]$(L= H_2O, pyridine). *J. Appl. Phys.* **2000**, *87*, 6007−6009.
(6) Kurmoo, M. Magnetic metal-organic frameworks. *Chem. Soc. Rev.* **2009**, *38*, 1353−1379.
(7) Shen, L.; Yang, S.-W.; Xiang, S.; Liu, T.; Zhao, B.; Ng, M.-F.; Göettlicher, J.; Yi, J.; Li, S.; Wang, L.; et al. Origin of Long-Range Ferromagnetic Ordering in Metal-Organic Frameworks with Antiferromagnetic Dimeric-Cu(II) Building Units. *J. Am. Chem. Soc.* **2012**, *134*, 17286.
(8) Jee, B.; Koch, K.; Moschkowitz, L.; Himsl, D.; Hartman, M.; Pöppl, A. Electron Spin Resonance Study of Nitroxide Radical Adsorption at Cupric Ions in the Metal-Organic Framework Compound $Cu_3(btc)_2$. *J. Phys. Chem. Lett.* **2011**, *2*, 357−361.
(9) Mendt, M.; Jee, B.; Himsl, D.; Moschkowitz, L.; Ahnfeldt, T.; Stock, N.; Hartmann, M.; Pöppl, A. A Continuous-Wave Electron Paramagnetic Resonance Study of Carbon Dioxide Adsorption on the Metal-Organic Frame-Work MIL-53. *Appl. Magn. Reson.* **2014**, *45*, 269−285.
(10) Chui, S. S.-Y.; Lo, S. M.-F.; Charmant, J. P.; Orpen, A. G.; Williams, I. D. A chemically functionalizable nanoporous material $[Cu_3(TMA)_2(H_2O)_3]_n$. *Science* **1999**, *283*, 1148−1150.
(11) Chowdhury, P.; Mekala, S.; Dreisbach, F.; Gumma, S. Adsorption of CO, CO_2 and CH_4 on Cu-BTC and MIL-101 metal organic frameworks: Effect of open metal sites and adsorbate polarity. *Microporous Mesoporous Mater.* **2012**, *152*, 246−252.
(12) Ferreira, A. F.; Santos, J. C.; Plaza, M. G.; Lamia, N.; Loureiro, J. M.; Rodrigues, A. E. Suitability of Cu-BTC extrudates for propane-propylene separation by adsorption processes. *Chem. Eng. J.* **2011**, *167*, 1−12.
(13) Šimėnas, M.; Kobalz, M.; Mendt, M.; Eckold, P.; Krautscheid, H.; Banys, J.; Pöppl, A. Synthesis, Structure, and Electron Paramagnetic Resonance Study of a Mixed Valent Metal-Organic Framework Containing Cu_2 Paddle-Wheel Units. *J. Phys. Chem. C* **2015**, *119*, 4898−4907.
(14) Pöppl, A.; Kunz, S.; Himsl, D.; Hartmann, M. CW and pulsed ESR spectroscopy of cupric ions in the metal-organic framework compound $Cu_3(BTC)_2$. *J. Phys. Chem. C* **2008**, *112*, 2678−2684.
(15) Kozachuk, O.; Khaletskaya, K.; Halbherr, M.; Bétard, A.; Meilikhov, M.; Seidel, R. W.; Jee, B.; Pöppl, A.; Fischer, R. A. Microporous Mixed-Metal Layer-Pillared $[Zn_{1-x}Cu_x(bdc)(dabco)_{0.5}]$ MOFs: Preparation and Characterization. *Eur. J. Inorg. Chem.* **2012**, *2012*, 1688−1695.
(16) EL Mkami, H.; Mohideen, M. I. H.; Pal, C.; McKinlay, A.; Scheimann, O.; Morris, R. E. EPR and Magnetic Studies of a Novel Copper Metal Organic framework (STAM-I). *Chem. Phys. Lett.* **2012**, *544*, 17.
(17) Arieli, D.; Prisner, T.; Hertel, M.; Goldfarb, D. Resolving Mn framework sites in large cage aluminophosphate zeotypes by high field EPR and ENDOR spectroscopy. *Phys. Chem. Chem. Phys.* **2004**, *6*, 172−181.
(18) Pospieszalski, M. W. Cylindrical Dielectric Resonators and Their Applications in TEM Line Microwave Circuits. *IEEE Trans. Microwave Theory Tech.* **1979**, *27*, 233−242.
(19) Jaworski, M.; Sienkiewicz, A.; Scholes, C. P. Double-Stacked Dielectric Resonator for Sensitive EPR Measurements. *J. Magn. Reson.* **1997**, *124*, 87−96.
(20) Blank, A.; Stavitski, E.; Levanon, H.; Gubaydullin, F. Transparent miniature dielectric resonator for electron paramagnetic resonance experiments. *Rev. Sci. Instrum.* **2003**, *74*, 2853−2859.
(21) Mattar, S. M.; ElNaggar, S. Y. Analysis of two stacked cylindrical dielectric resonators in a TE102 microwave cavity for magnetic resonance spectroscopy. *J. Magn. Reson.* **2011**, *209*, 174−182.
(22) Friedländer, S.; Ovchar, O.; Voigt, H.; Böttcher, R.; Belous, A.; Pöppl, A. Dielectric Ceramic EPR Resonators for Low Temperature Spectroscopy at X-band Frequencies. *Appl. Magn. Reson.* **2015**, *46*, 33−48.
(23) Stoe & Cie GmbH, XRD Analysis. Darmstad, 2006.
(24) Brandenburg, K. *Diamond 3.0*; Crystal Impact GbR: Bonn, 2004.
(25) Belous, A.; Ovchar, O.; Valant, M.; Suvorov, D. Abnormal behavior of the dielectric parameters of $Ba_{6-x}Ln_{8+2x/3}Ti_{18}O_{54}$ (Ln= La-Gd) solid solutions. *J. Appl. Phys.* **2002**, *92*, 3917−3922.
(26) Stoll, S.; Schweiger, A. EasySpin, a comprehensive software package for spectral simulation and analysis in EPR. *J. Magn. Reson.* **2006**, *178*, 42−55.
(27) Carl, P. J.; Larsen, S. C. EPR study of copper-exchanged zeolites: effects of correlated g-and A-Strain, Si/Al Ratio, and Parent zeolite. *J. Phys. Chem. B* **2000**, *104*, 6568−6575.
(28) The real part of of the magnetic susceptibility, χ', causes EPR signal dispersion, the imaginary part χ'' absorption. χ'' is recorded in a cw EPR mw absorption experiment, technically as the first derivative $d\chi''/dB$ via the time modulated field $\mathbf{B}_0(t)$. This quantity is the common cw EPR measurement parameter given in all plots in arbitrary units.
(29) Eaton, G. R.; Eaton, S. S.; Barr, D. P.; Weber, R. T. *Quantitative EPR*; Springer Science & Business Media: Amsterdam, 2010.
(30) Abragam, A.; Bleaney, B. *EPR of Transition Ions*; Clarendon Press: Oxford, 1970.
(31) Kahn, O. Dinuclear complexes with predictable magnetic properties. *Angew. Chem., Int. Ed. Engl.* **1985**, *24*, 834−850.
(32) Jee, B.; Eisinger, K.; Gul-E-Noor, F.; Bertmer, M.; Hartmann, M.; Himsl, D.; Pöppl, A. Continuous Wave and Pulsed Electron Spin Resonance Spectroscopy of Paramagnetic Framework Cupric Ions in the Zn(II) Doped Porous Coordination Polymer $Cu_{3-x}Zn_x(btc)_2$. *J. Phys. Chem. C* **2010**, *114*, 16630−16639.
(33) Hathaway, B.; Billing, D. The electronic properties and stereochemistry of mono-nuclear complexes of the copper (II) ion. *Coord. Chem. Rev.* **1970**, *5*, 143−207.
(34) Tominaga, H.; Ono, Y.; Keii, T. Spectroscopic study of Cu (II) ions supported on silica gel by cation exchange method. *J. Catal.* **1975**, *40*, 197−202.
(35) Kevan, L. Electron spin echo studies of the location and coordination of metal species on oxide surfaces. *Acc. Chem. Res.* **1987**, *20*, 1−7.
(36) Sakaguchi, U.; Addison, A. W. Spectroscopic and redox studies of some copper (II) complexes with biomimetic donor atoms: implications for protein copper centres. *J. Chem. Soc., Dalton Trans.* **1979**, 600−608.
(37) Jee, B.; St. Petkov, P.; Vayssilov, G. N.; Heine, T.; Hartmann, M.; Pöppl, A. A Combined Pulsed Electron Paramagnetic Resonance Spectroscopic and DFT Analysis of the $^{13}CO_2$ and ^{13}CO Adsorption

DOI: 10.1021/acs.jpcc.5b05019
J. Phys. Chem. C 2015, 119, 19171−19179

on the Metal-Organic Framework $Cu_{2.97}$ $Zn_{0.03}(btc)_2$. *J. Phys. Chem. C* **2013**, *117*, 8231−8240.

DOI: 10.1021/acs.jpcc.5b05019
J. Phys. Chem. C 2015, 119, 19171−19179